Geophys. J. R. astr. Soc. (1987) **88,** 277–296

A stable finite element solution for two-dimensional magnetotelluric modelling

Philip E. Wannamaker and John A. Stodt *Earth Science Laboratory, University of Utah Research Institute, 391 Chipeta Way, Suite C, Salt Lake City, Utah 84108-1295, USA*

Luis Rijo *Universidade Federal Do Para, Campus Universitario Do Guama, Belem-Para-Brasil, CP 1611, Brazil*

Accepted 1986 August 1. Received 1986 August 1; in original form 1985 November 11

Summary. We report herein on a finite element algorithm for 2-D magnetotelluric modelling which solves directly for secondary variations in the field parallel to strike, plus the subsequent vertical and transverse auxiliary fields, for both transverse electric and transverse magnetic modes. The governing Helmholtz equations for the secondary fields along strike are the same as those for total field algorithms with the addition of source terms involving the primary fields and the conductivity difference between the body and the host. Our approach has overcome a difficulty with numerical accuracy at low frequencies observed in total field solutions with 32-bit arithmetic for the transverse magnetic mode especially, but also for the transverse electric mode. Matrix ill-conditioning, which affects total field solutions, increases with the number of element rows with the square of the maximum element aspect ratio and with the inverse of frequency. In the secondary formulation, the field along strike and the auxiliary fields do not need to be extracted in the face of an approximately computed primary field which increasingly dominates the total field solution towards low frequencies. In addition to low-frequency stability, the absolute accuracy of our algorithm is verified by comparison with the TM and the TE mode analytic responses of a segmented overburden model.

Key words: magnetotellurics, finite elements, ill-conditioning

Introduction

The finite element method has been applied to the problem of electromagnetic scattering in a heterogeneous earth for more than a decade, and the solution at least for magnetotelluric (MT) fields over two-dimensional (2-D) structures is widely considered to be well in hand (e.g. Coggon 1971; Ward, Peoples & Ryu 1973; Kisak & Sylvester 1975; Rijo 1977). The

plane-wave source algorithms for 2-D bodies, with the exception of that by Coggon (1971), typically solve for the total field parallel to strike (E_x for the transverse electric mode, H_x for the transverse magnetic mode), from which the auxiliary vertical and transverse to strike fields are computed through difference approximations to Maxwell's equations. Finite difference and related algorithms for this problem take a similar approach (e.g. Swift 1967; Brewitt-Taylor & Weaver 1976).

As demonstrated in this paper, finite element programs which solve for total fields unfortunately suffer numerical inaccuracy especially towards low frequencies due to the finite length of the computer word. This difficulty is more severe for the transverse magnetic (TM) results than for the transverse electric (TE), but both modes exhibit gross errors towards very low frequencies on 32-bit (single precision) computing machines. Coggon (1971) recommended solving directly for the secondary field variations, to increase accuracy where the secondary component is much less than the total, and presented results for induced polarization and TE electromagnetics. We present a secondary formulation for both TE and TM modes of the MT technique and show that it provides stable and accurate results to ultralow frequencies for single precision arithmetic.

Method of solution

The secondary formulation utilized by Coggon (1971) necessitates construction of finite element matrix equations for the total conductivity distribution and for the anomalous distribution (i.e. that departing from the 1-D host), and then multiplication of the latter by the vector of primary fields at the element nodes to obtain the source vector for the secondary fields. We give, instead, the differential equations for the secondary fields directly as this leads to a more straightforward derivation of the element equations.

GOVERNING DIFFERENTIAL EQUATIONS

Following Hohmann (1983), the electric and magnetic fields in and around an inhomogeneity in the earth are separated into a primary component, representing fields in the 1-D host when the body is absent, and a secondary component resulting from the body. Defined in a manner suitable for differential analysis, Maxwell's equations giving the secondary components of the TE mode for 2-D geometries are

$$\frac{\partial E_{xs}}{\partial z} = -\hat{z} H_{ys}, \tag{1}$$

$$\frac{\partial E_{xs}}{\partial y} = \hat{z} H_{zs}, \tag{2}$$

and

$$\frac{\partial H_{zs}}{\partial y} - \frac{\partial H_{ys}}{\partial z} = \hat{y} E_{xs} + \Delta\hat{y} E_{xp}, \tag{3}$$

where $\hat{y} = \sigma + i\omega\epsilon$ is admittivity, $\hat{z} = i\omega\mu_0$ is impedivity, $\Delta\hat{y}$ is the admittivity difference between the 2-D inhomogeneity and its 1-D host, and subscripts s and p refer to secondary and primary (1-D earth) field components. We use an $\exp(i\omega t)$ time dependence and z is positive downward. Conductivity, dielectric permittivity and free space magnetic permeability (assumed throughout) are σ, ϵ, and μ_0 while ω is angular frequency. Substituting (1)

and (2) into (3) and rearranging, the TE Helmholtz equation is

$$\frac{\partial}{\partial y}\left(\frac{1}{\hat{z}}\frac{\partial E_{xs}}{\partial y}\right)+\frac{\partial}{\partial z}\left(\frac{1}{\hat{z}}\frac{\partial E_{xs}}{\partial z}\right)-\hat{y}E_{xs}=\Delta\hat{y}E_{xp}. \tag{4}$$

Similarly, Maxwell's equations for the secondary components of the TM mode are

$$\frac{\partial H_{xs}}{\partial z}=\hat{y}E_{ys}+\Delta\hat{y}E_{yp}, \tag{5}$$

$$\frac{\partial H_{xs}}{\partial y}=-\hat{y}E_{zs}-\Delta\hat{y}E_{zp}, \tag{6}$$

and

$$\frac{\partial E_{zs}}{\partial y}-\frac{\partial E_{ys}}{\partial z}=-\hat{z}H_{xs}. \tag{7}$$

Substituting (5) and (6) into (7), the TM Helmholtz equation is

$$\frac{\partial}{\partial y}\left(\frac{1}{\hat{y}}\frac{\partial H_{xs}}{\partial y}\right)+\frac{\partial}{\partial z}\left(\frac{1}{\hat{y}}\frac{\partial H_{xs}}{\partial z}\right)-\hat{z}H_{xs}=-\frac{\Delta k^2}{\hat{y}}H_{xp}+\frac{\partial}{\partial z}\left(\frac{\Delta\hat{y}}{\hat{y}}\right)E_{yp}, \tag{8}$$

where $\Delta k^2=-\Delta\hat{y}\hat{z}$ and E_{zp} is zero in the MT technique.

The Helmholtz equations for the secondary fields are the same as those for the total fields with the addition of source terms involving the primary fields and the conductivity difference between the body and the host. Thus, different finite element matrix equations do not need to be worked out but instead we just need to derive the appropriate source vector entries, which are the inner products of the sources of (4) and (8) with the element shape functions described shortly. For the TM modes, the source term involving E_{yp} is a surface current distribution in the strike direction along the boundaries of the inhomogeneity (Hohmann 1983) and in the low-frequency limit provides the galvanic or boundary charge contribution to the response (Wannamaker, Hohmann & Ward 1984). A similar term involving H_{yp} would appear for the TE mode if magnetic permeability gradients were allowed.

FINITE ELEMENT SOLUTION

Application of finite elements to EM scattering is described in the previous citations and pertinent general references on the method include, e.g. Strang & Fix (1973) and Huebner & Thornton (1982). Our description therefore will be brief and particular to our secondary field formulation, with a detailed presentation appearing in Wannamaker, Stodt & Rijo (1985).

We employ a mesh design comprised of rectangular elements, of constant width in a given element column and constant height in a given element row (Fig. 1). The rectangular elements moreover consist of four triangular elements within each of which the admittivity and impedivity are constant. This construction eases coding and model input yet allows simulation of sloping boundaries. The unknown secondary field parallel to strike is approximated by piece-wise linear functions defined over each triangular subregion. The field is specified using three linear shape functions, whose amplitudes in turn are unity at one node (corner) of the subregion and zero at the other two nodes (Strang & Fix 1973, p. 138; Hohmann 1983; Wannamaker *et al.* 1985). By setting the inner product of the approximation error with the shape functions to zero over the triangular element (e.g. Huebner &

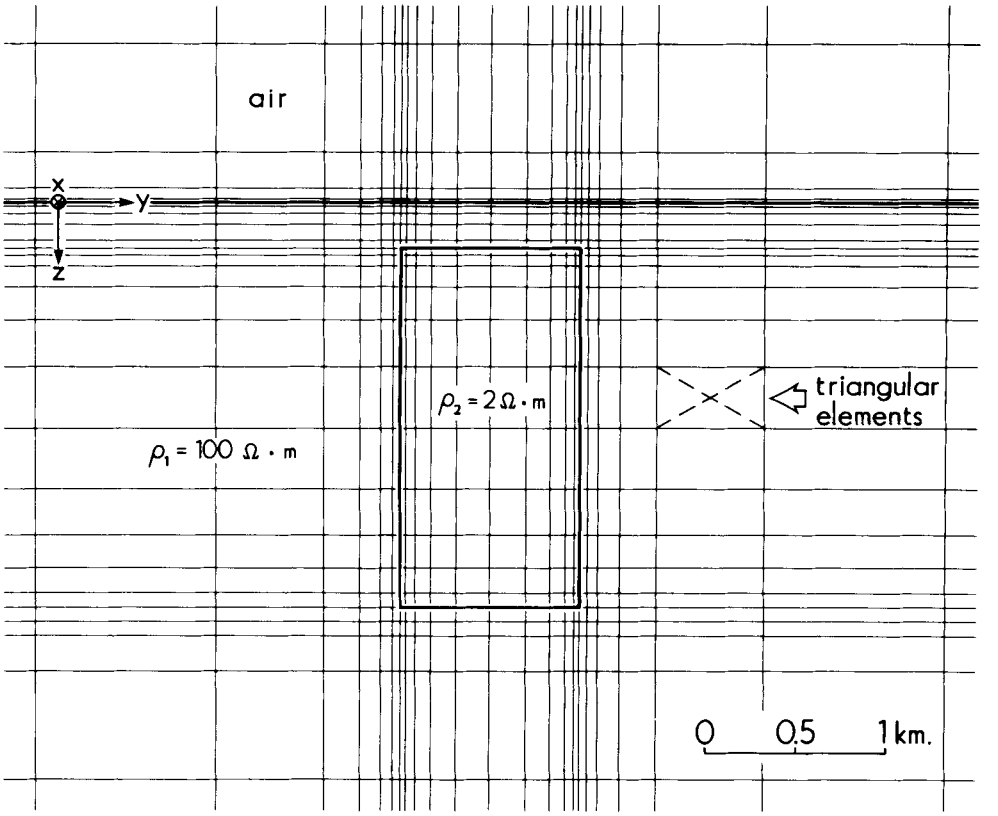

Figure 1. Central portion of mesh describing conductive vertical prism in resistive half-space. The very large outer rows and columns of elements stated in the text could not be shown in this figure due to their size.

Thornton 1982, p. 110), a 3 x 3 local element matrix results giving the field values f_i, f_j, f_k at the three nodes i, j, k in terms of the element dimensions and properties. This matrix equation is

$$\left[\frac{-1}{4q\Delta}\begin{pmatrix} b_i^2+c_i^2 & b_ib_j+c_ic_j & b_ib_k+c_ic_k \\ & b_j^2+c_j^2 & b_jb_k+c_jc_k \\ & & b_k^2+c_k^2 \end{pmatrix} + \frac{p\Delta}{12}\begin{pmatrix} 2 & 1 & 1 \\ 1 & 2 & 1 \\ 1 & 1 & 2 \end{pmatrix}\right]\begin{bmatrix} f_i \\ f_j \\ f_k \end{bmatrix} = \begin{bmatrix} S_i \\ S_j \\ S_k \end{bmatrix}, \qquad (9)$$

where $q = \hat{z}_0$, $p = -\hat{y}$ for the TE mode and $q = \hat{y}$, $p = -\hat{z}_0$ for TM mode. The area of the triangular element is Δ. Other entries of the matrix are $b_i = z_j - z_k$, $c_i = y_j - y_k$, with the rest obtained through cyclic permutation of i, j, k.

The entries of the source vector depend upon whether the TE or TM mode is being considered. The volume terms of the sources of both TE and TM modes are integrated readily using the approximation that the primary field is constant within each triangular element. The primary field is evaluated at the centroid of each triangular area (depths $z_1 - z_4$ in Fig. 2). The surface term of the TM source of (8), however, enters into the matrix equations as a line integral along each element boundary of the product of $(\Delta\hat{y}/\hat{y})/E_{yp} \sin\theta$, where θ is the angle clockwise from the $+y$-axis to a vector in the direction of the anomalous

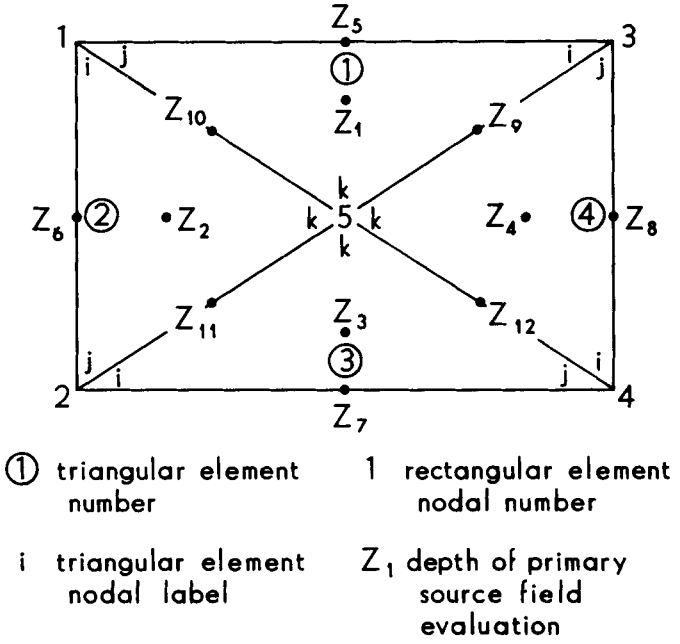

Figure 2. Triangular and rectangular element nodal ordering conventions and evaluation points of primary source fields (depths z_1–z_{12}). For strictly rectangular elements, $z_6 = z_8$, $z_9 = z_{10}$, and $z_{11} = z_{12}$.

admittivity gradient, and the variation of the shape functions around their edges. The primary field again is assumed constant along each triangular element boundary and is calculated at the boundary midpoints (depths z_5–z_{12} in Fig. 2). The entries of the 3×1 source vectors for both modes are as follows:

$$\begin{bmatrix} S_i^{\mathrm{TE}} \\ S_j^{\mathrm{TE}} \\ S_k^{\mathrm{TE}} \end{bmatrix} = \frac{\Delta}{3} \begin{bmatrix} \Delta\hat{y}_1 E_{xp1} \\ \Delta\hat{y}_1 E_{xp1} \\ \Delta\hat{y}_1 E_{xp1} \end{bmatrix}, \tag{10a}$$

$$\begin{bmatrix} S_i^{\mathrm{TM}} \\ S_j^{\mathrm{TM}} \\ S_k^{\mathrm{TM}} \end{bmatrix} = -\frac{\Delta}{3} \begin{bmatrix} \dfrac{\Delta k_1^2}{\hat{y}_1} H_{xp1} \\ \dfrac{\Delta k_1^2}{\hat{y}_1} H_{xp1} \\ \dfrac{\Delta k_1^2}{\hat{y}_1} H_{xp1} \end{bmatrix} + \frac{1}{4} \begin{bmatrix} \dfrac{2\Delta\hat{y}_1}{\hat{y}_1} c_k E_{yp5} + \dfrac{\Delta\hat{y}_1}{\hat{y}_1} c_j E_{yp9} \\ \dfrac{2\Delta\hat{y}_1}{\hat{y}_1} c_k E_{yp5} + \dfrac{\Delta\hat{y}_1}{\hat{y}_1} c_i E_{yp10} \\ \dfrac{\Delta\hat{y}_1}{\hat{y}_1} c_j E_{yp9} + \dfrac{\Delta\hat{y}_1}{\hat{y}_1} c_i E_{yp10} \end{bmatrix}, \tag{10b}$$

where c_i, c_j, c_k have the same definitions as for equation (9). The simplicity of the boundary terms of the TM source results because the hypotenuse of the sine cancels the length of this boundary integration. Also, the primary field and physical property values indicated in equation (10) are for triangular element 1 of Fig. 2 and would be replaced appropriately for the other three subregions.

The element equations for the four triangular subregions of the rectangular element are next loaded additively into a 5×5 matrix equation describing the field variations over the

rectangle. This 5 x 5 equation is spelled out in Wannamaker *et al.* (1985). The locations of the matrix entries are according to the rectangular element nodal numbers shown in Fig. 2. Finally, the field variable associated with the internal node of the rectangular element is eliminated via static condensation (Huebner & Thornton 1982). The resulting 4 x 4 element matrices and corresponding 4 x 1 sources for each rectangle are assembled additively in the global matrix for reduction. The position of the matrix terms here is dictated by the global node numbering scheme, whereby the upper left node of the mesh is the first and the remainder increment down the left nodal column, continuing column by column to the right, and ending with the lower right node of the mesh. This definition gives rise to a symmetric, banded matrix well known in the finite element method (Huebner & Thornton 1982).

Dirichlet boundary conditions are normally applied at all external mesh boundaries when solving the magnetotelluric problems. By convention, the earth layering on the left side of the mesh is taken as the host layering for anomalous conductivity. Since the mesh is designed so that its edges are remote from the conductivity inhomogeneity, zero boundary conditions are imposed at the left edge. However, if the earth layering at the right edge differs from that at the left, then inhomogeneity and sources can be considered to extend indefinitely to the right and non-zero boundary conditions apply. For the TM mode, the right-side boundary values now become the differences between the layered earth fields of the 1-D sequences at the right and left edges of the mesh. The values at the right corners of the mesh are extended to the left with a cosine taper to give the boundary conditions along the top and bottom of the mesh. For TE mode boundary conditions in the air, however, the arctangent behaviour given by Brewitt-Taylor & Weaver (1976) is used, which preserves matrix symmetry. The boundary conditions are now prescribed directly in the global system with appropriate modification of the source vector (Huebner & Thornton 1982, p. 52). This method decreases time-consuming underflows during matrix reduction relative to simply assigning large weights to boundary values (Huebner & Thornton 1982). The reduction is done using Gaussian elimination specialized to banded, symmetric matrices.

From the secondary field parallel to strike obtained by solution of the global matrix, the auxiliary secondary fields vertical and transverse to strike obtain through a numerical approximation to Maxwell's equations (1) and (2) for the TE mode and (5) and (6) for the TM mode. The appropriate derivatives are evaluated numerically by fitting piecewise parabolas to three adjacent mesh field values and taking the derivative according to the coefficients of the fit. Subsequently, the primary E- and H-fields (from the left edge layering) are added to the computed secondary fields. The nodal values of the field parallel to strike used in differentiation are kept within the earth and for the TM mode are kept from straddling resistivity discontinuities below surface. If the nodal values require shifting for this purpose, the derivatives are evaluated at the endpoints rather than the midpoints of the parabolas to yield the fields at the receiver locations of interest (Wannamaker *et al.* 1986). An additional wavenumber term provided by Weaver, Le Quang & Fischer (1986) is used for the TE mode if the nodes cross lateral resitivity contacts in the earth.

Example calculations

In this section we verify our secondary field solution. To compare its stability with that of the total field approach, and to illustrate the source of error in the total fields, a conductive prism in a half-space is considered. Subsequently, an analytic solution for a segmented overburden model is used to show the absolute accuracy possible with the secondary field method.

RESPONSE OF CONDUCTIVE PRISM

A simple vertical prism is shown in Fig. 1 along with the finite element discretization in its immediate vicinity. The prism is of low resistivity ($2\ \Omega\ m^{-1}$) relative to its host ($100\ \Omega\ m^{-1}$). As distance increases from the body in both vertical and horizontal directions, element sizes progress in a series 300, 1000, . . . , 100 000 m. A total of 37 nodal columns ($ny = 37$) and 35 nodal rows ($nz = 35$) define the mesh for the TE mode. With the air layer removed, 26 nodal rows define the mesh for the TM mode. Calculations were performed using the secondary fields formulation described herein on a PRIME 2655 minicomputer as well as using an earlier total fields version of the algorithm (Stodt 1978) on the PRIME 2655 and on a UNIVAC 1100/61 computer. The PRIME 2655 employs 32 bits of floating point numerical representation while the UNIVAC uses 36 bits, with three of the additional four bits devoted to the mantissa. Both machines truncate rather than round the extra guard bits following an arithmetic operation. All codes were compiled in FORTRAN 77.

The following description of responses applies specifically to the secondary field formulation, which as discussed shortly is considered the most accurate of the calculations presented. At high frequencies, apparent resistivity ρ_{xy} in Fig. 3 shows a local minimum

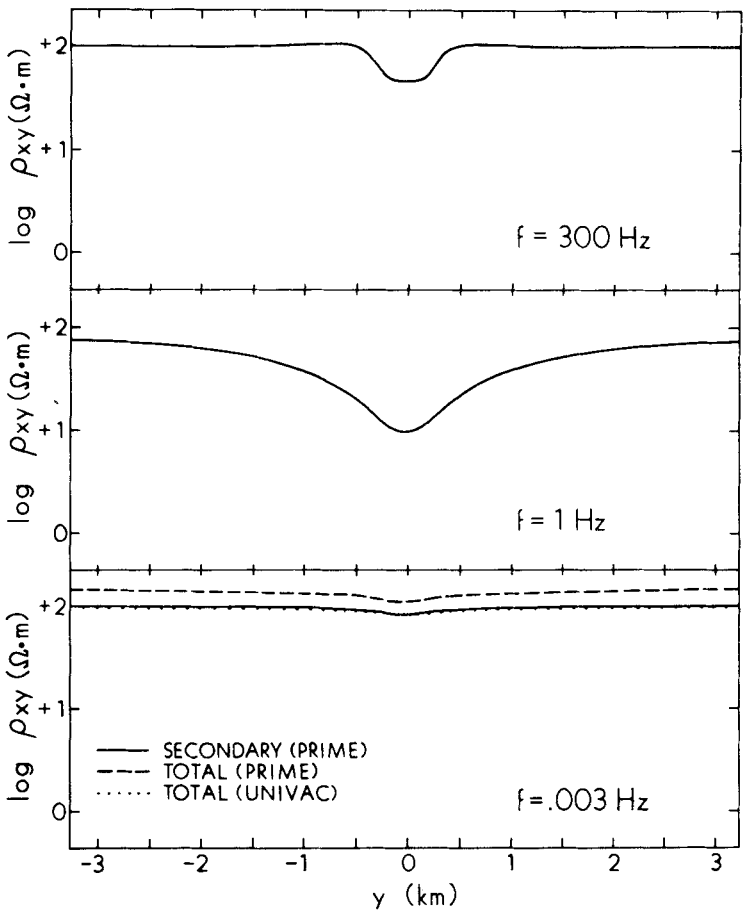

Figure 3. TE apparent resistivity ρ_{xy} at three frequencies over the conductive prism calculated using the secondary and total field versions of the algorithm as executed on the PRIME and the UNIVAC.

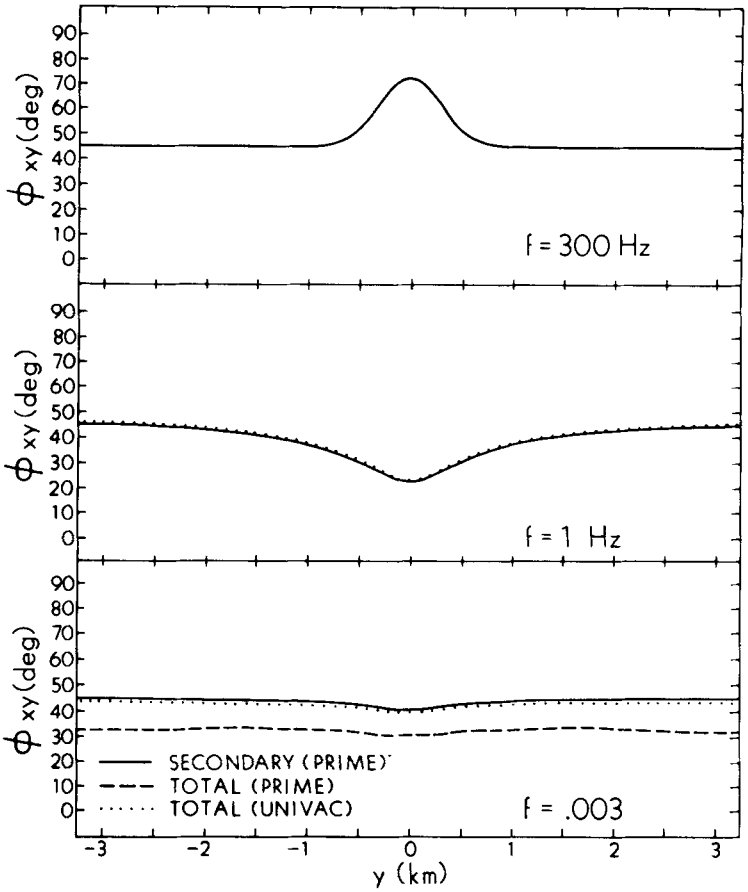

Figure 4. TE impedance phase ϕ_{xy} at three frequencies over the conductive prism calculated using the secondary and total field versions of the algorithm as executed on the PRIME and the UNIVAC.

right over the conductor with very slight maxima just outside. The anomaly has progressed to a broad low over and outside the conductor by 1 Hz and, as frequency diminishes further, the anomaly decays to a small depression below 100 Ω m^{-1}. In a complementary manner, impedance phase ϕ_{xy} in Fig. 4 shows a positive anomaly at 300 Hz over the conductor, but is less than 45° (the phase of the half-space response) at frequencies of 1 Hz and below as ρ_{xy} returns toward 100 Ω m^{-1}. The attenuation of the TE anomaly as frequency becomes low corresponds to the differential component of the Helmholtz operator in (4) dominating the remaining terms, including the source for the secondary electric field (see Wannamaker *et al.* 1984). The small TE response at low frequencies in fact is due to a secondary magnetic field resulting from excess currents within the prism.

The transverse magnetic results of Figs 5 and 6 differ markedly from those transverse electric. At 300 Hz, ρ_{yx} in Fig. 5 is low right over the conductor and returns monotonically to the background apparent resistivity with distance. At 1 Hz and below, a striking minimum in ρ_{yx} has developed over the body with positive departures from 100 Ω m^{-1} appearing outside. This anomaly pattern increases toward a maximum as frequency falls. In Fig. 6 at 300 Hz, ϕ_{yx} shows a strong positive anomaly over the conductor similar to ϕ_{xy} but of

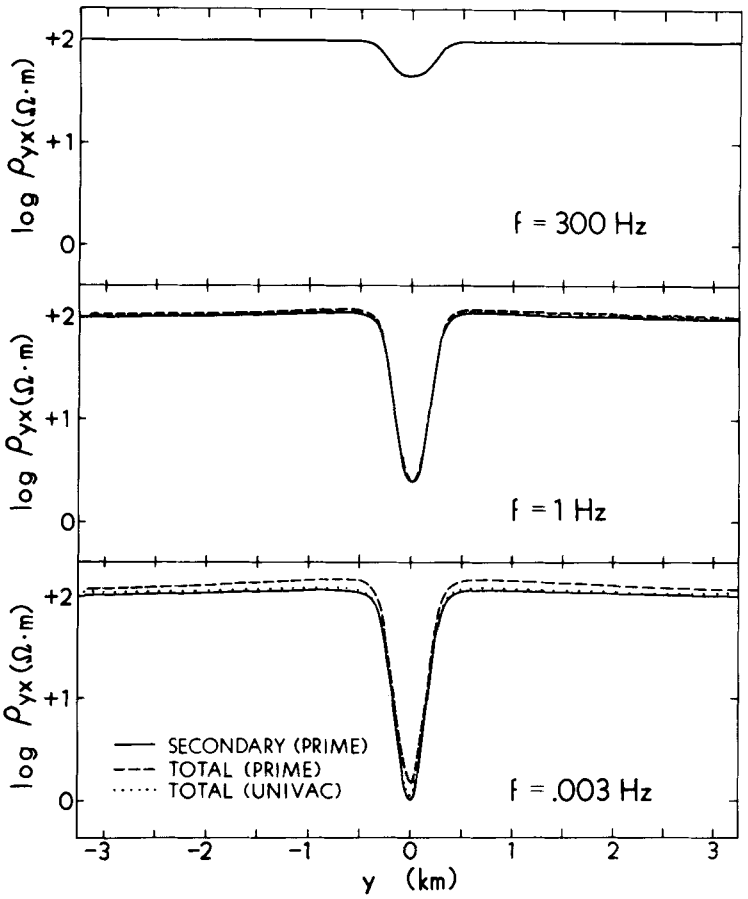

Figure 5. TM apparent resistivity ρ_{yx} at three frequencies over the conductive prism calculated using the secondary and total field versions of the algorithm as executed on the PRIME and the UNIVAC.

narrower lateral extent. This anomaly pattern diminishes in amplitude as frequency decreases. Slight negative departures in ϕ_{yx} from 45° outside the inhomogeneity are most obvious at mid frequencies. That an approximately electric dipolar form to the apparent resistivity anomaly develops as frequency falls is a result of electric charge on the boundaries of the prism which occurs to preserve total current flow normal to the boundaries (Wannamaker *et al.* 1984). The impedance phase response approaches 45° at low frequencies because there only the surface current remains as the source to the low frequency limit (differential component) of the Helmholtz operator (4).

Differences can be seen between the results of the secondary and total field formulations executed on the PRIME. They are indiscernible at high frequencies, slight at 1 Hz, but become large at low frequencies. The impedance phases differ somewhat more than the apparent resistivities. For the TM mode, these total field results are not even symmetrical across the axis of the conductor and ϕ_{yx} shows anomalous character over the body which is of the opposite sense to that of the secondary field calculation. At 10^{-5} Hz (not shown), ϕ_{xy} from the total field solution on the PRIME lies in the absurd vicinity of −65° to −70° while ρ_{xy} is very erratic but generally ranges from 20 to 50 Ω m^{-1}. Also, ϕ_{yx} has fallen to around

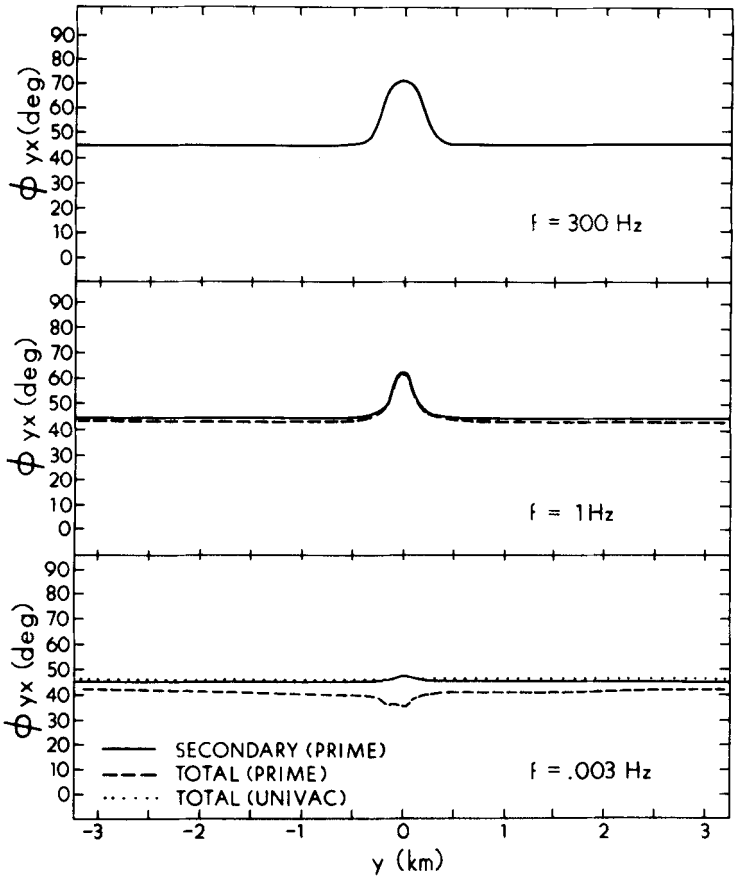

Figure 6. TM impedance phase ϕ_{yx} at three frequencies over the conductive prism calculated using the secondary and total field versions of the algorithm as executed on the PRIME and the UNIVAC.

5°–10° while ρ_{yx} averages a full order of magnitude greater than that of the secondary field solution. The total field results on the UNIVAC remain fairly close to the secondary field calculations on the PRIME at the three frequencies shown, with the largest discrepancy occurring again at the lowest frequency. At 10^{-5} Hz, ϕ_{xy} from the UNIVAC total field solution lies near 48° with ρ_{xy} around 90 Ω m^{-1}. For the TM mode from the UNIVAC, ϕ_{yx} has dropped below 40° overall, but with a particular low about 24° right over the conductor, while ρ_{yx} on the whole is about a factor of two larger than the secondary field results.

Since identical total field codes were compiled on the PRIME and the UNIVAC, we believe that the secondary field formulation is more accurate and that the discrepancies displayed with the total field method arise from the difference in numerical precision between the two machines. The secondary field algorithm run on the UNIVAC agreed with that on the PRIME to within 0.1 per cent magnitude and 0.1° phase at all frequencies. At 10^{-5} Hz, the secondary field formulation on both machines provides a precise low frequency estimate of the response. Here, ϕ_{xy} and ρ_{xy} reach the values 44.7° and 99.1 Ω m^{-1} directly over the conductor. Moreover, a value of ϕ_{yx} of 45.1° and a low in ρ_{yx} of 9.59 Ω m^{-1} occur over the body. The secondary field results on the PRIME remain completely stable for both modes even at 10^{-8} Hz.

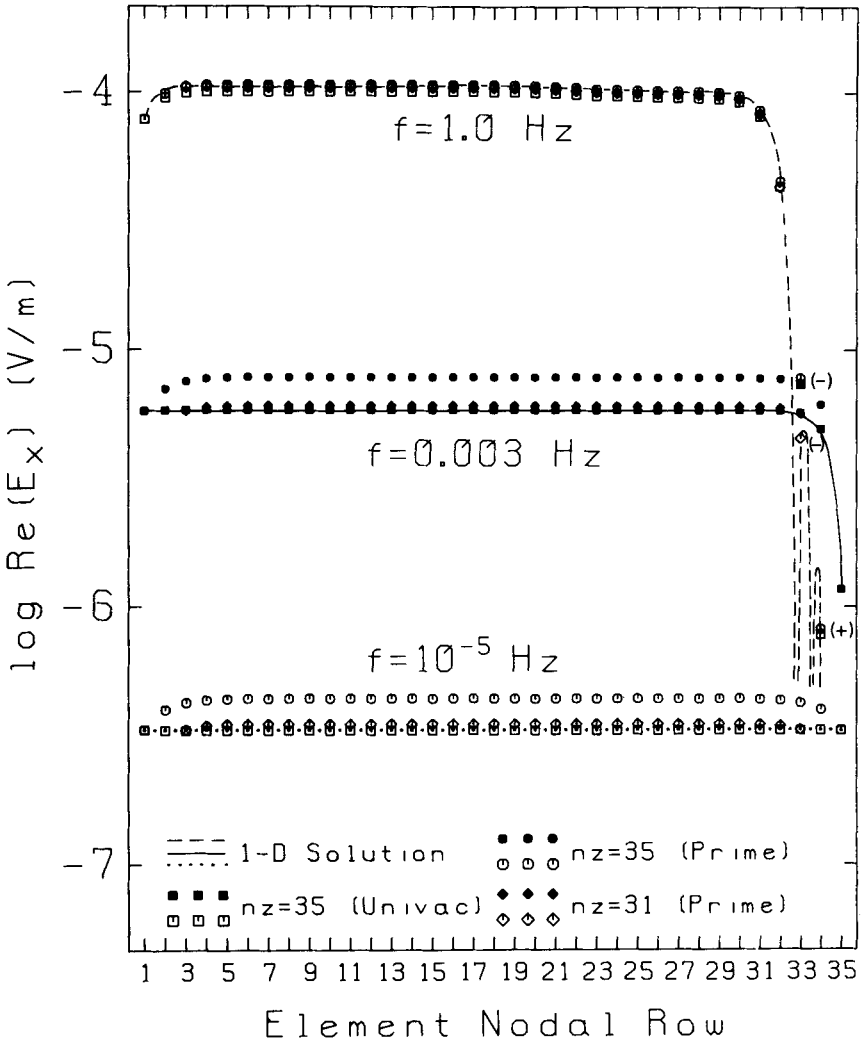

Figure 7. Real component of TE mode electric fields at three frequencies down central nodal column of mesh of Fig. 1 with prism set to 100 Ω m^{-1} (i.e. a half-space is simulated). Variable *nz* is the number of nodes in the vertical dimension of the mesh. The air–earth interface is at nodal row nine. The relation between *nz* and depth is neither linear nor log-linear; e.g. node 21 is at 0.625 km depth while node 32 is at 5.6 km depth.

ERROR IN THE TOTAL FIELD APPROACH

With Figs 7 and 8 we take a closer look at the total field inaccuracy. Here at frequencies of 1, 0.003 and 10^{-5} Hz we plot the real part of the electric field parallel to strike (TE mode) and perpendicular to strike (TM mode) down the central nodal column of the mesh of Fig. 1, but where just a 100 Ω m^{-1} half-space is simulated. To compare with the TE finite element results, analytic values for E_x in the uniform earth are plotted in Fig. 7 as well. The electric field across strike in Fig. 8 was calculated again by fitting parabolas to groups of three adjacent nodal values of the H-field parallel to strike. It also was performed on the analytic half-space solution for H_x at the nodes to obtain the '1-D' solution for E_y.

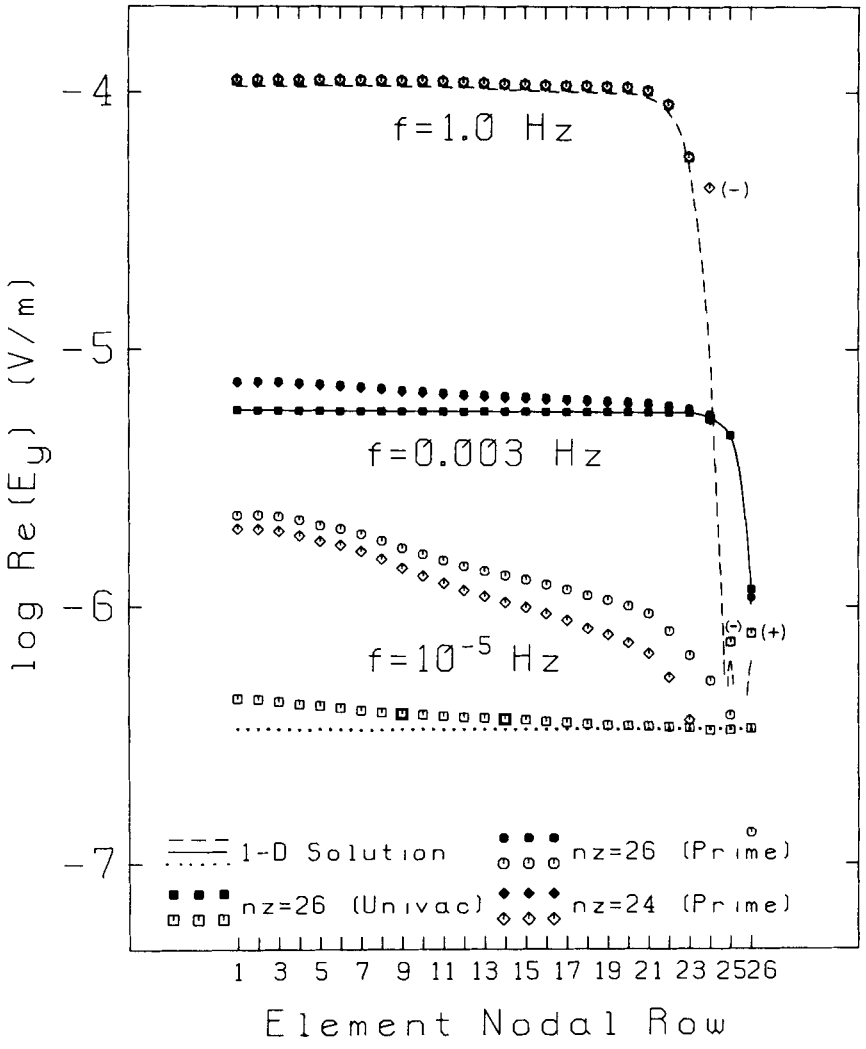

Figure 8. Real component of TM mode electric fields at three frequencies down central nodal column of mesh of Fig. 1 with prism set to 100 Ω m^{-1} (i.e. a half-space is simulated). The air–earth interface now is at nodal row one. Node 12 is at 0.625 km depth while node 23 is at 5.6 km depth.

Discrepancies between this half-space E-field and that from finite elements thus should reflect solely the numerical imprecision in the finite element solution. A comparison of Figs 7 and 8 indicates that estimating the 1-D E_y from H_x using the parabolic approximation is not very accurate at higher frequencies if the fields are oscillatory. Finally, in addition to this half-space mesh, one with the outer two rows of elements, of heights 30 and 100 km, removed (nz = 31) was modelled.

At 1 Hz, the total field solutions on the PRIME (both nz = 31 and nz = 35) and on the UNIVAC agree well with the analytic values for both TE and TM modes. Remarkably, even at the lowest nodes of the mesh where the solution is oscillatory, the element subdomain variations track the true response very well. At 0.003 Hz in Fig. 7, the total field solution for E_x (TE) on the UNIVAC with nz = 35 has remained accurate but that on the PRIME shows

an upward distortion from the analytic response that occurs within a few nodes of the boundaries, which have retained the proper values through the course of matrix solution. The onset of this error has a similar appearance if one examines fields along an element nodal row across the mesh. At 10^{-5} Hz, the analytic results are essentially constant down the entire nodal column, but the upward bias in the finite element computation of E_x on the PRIME remains. The percentage error in the calculation of E_x, more importantly in the slope of E_x with depth, thus reaches a low-frequency limit by 10^{-5} Hz. Since the auxiliary total magnetic field normal to strike and computed from this slope of E_x is weighted by the inverse of frequency through Maxwell's equations, the percentage error in impedance and thus in apparent resistivity and phase increases as frequency falls as exemplified in Figs 3 and 4.

A similar bias in H_x, and in its slope with depth, develops towards a low-frequency limit for the TM mode (Fig. 8). Although this bias is only of the order of 0.2 per cent of the true values of H_x, when the auxiliary electric field E_y normal to strike is computed, an erroneously large value obtains which also becomes nearly constant at very low frequencies. This is in contrast to the true half-space E_y which decreases according to $\sqrt{\omega}$. Therefore, the percentage error in apparent resistivity and impedance phase for the TM mode also becomes arbitrarily large as frequency approaches zero. The error in slope of H_x (also in slope of E_x) occurs more in the real than in the imaginary, thus accounting for the impedance phase approaching very small values at very low frequencies. Furthermore, reducing the number of nodal rows to $nz = 31$ has improved the TM solution on the PRIME substantially less than for the TE calculations of Fig. 7.

Additional mesh geometries have been experimented with. For instance, five more rows of elements were added to the top and bottom of the mesh so that the outermost rows were 3000 km high and $nz = 45$. On the PRIME, the computed magnitudes of E_x exceeded those of the true 1-D values by more than a factor of 10 and the signs of both real and imaginary components were reversed. This maximum distortion was reached for frequencies below about 10^{-6} Hz. Commensurately bad results occurred for the TM mode. Curiously, the solution of this large mesh on the UNIVAC was only about a factor of two worse than that shown in Figs 7 and 8, although the apparent resistivities and phases at low frequencies still were grossly wrong due to auxiliary field errors. Differences between the two machines in word normalization procedures or in the supporting Fortran 77 library may be important here. Core limitations on the UNIVAC (256 K words) prohibited testing of larger meshes.

Criteria for development of serious computer round-off errors in finite elements are reviewed by Strang & Fix (1973, Ch. 5). By their methods, an upper bound on the ill-conditioning of the global matrix for the 2-D EM Helmholtz operator varies according to the value of nz, the ratio squared of the maximum and minimum element dimensions in the mesh, and the inverse of frequency. A lower bound is similar but does not involve frequency. We believe these criteria explain much of the error behaviour shown in Figs 7 and 8 and in our other test meshes. Other factors are important, however. Specifically, when the matrix elements were computed in single precision, but then loaded into double precision arrays for reduction with the resulting fields truncated to 32 bits, the total E_x for the TE mode agreed well with the analytic solution at low frequencies, but the error in E_y for the TM mode total solution diminished by only about 25 per cent. It is important that the secondary field parallel to strike, which becomes a vanishingly small fraction of the total field toward low frequencies, is represented accurately in the auxiliary field calculation and this appears impossible beyond a certain point for total field solutions in single precision.

This discussion is not intended as harsh criticism of any particular computing machine. The secondary field formulation advocated herein provides precise results to ultralow

frequencies using single precision arithmetic on either the PRIME or the UNIVAC. That this formulation performs so well is due it seems to two reasons. First, the secondary solution normally is zero near the boundaries of the mesh where extreme elements reside and is driven by sources concentrated over the inhomogeneity, so that a large total field does not need to be propagated very precisely over the entire mesh during matrix reduction. Second, the auxiliary fields are computed directly from the secondary field parallel to strike and thus do not need to be extracted in the face of an approximate and increasingly dominant primary field.

COMPARISON WITH ANALYTIC MODEL

As a final exercise, we check the absolute accuracy of our formulation against the analytic response of a 50 km thick segmented overburden on a perfectly conducting basement for a period of 300 s (Fig. 9). The TM mode of this model has been considered by Weaver, LeQuang & Fischer (1985) and the finite element discretization we employ is the same as for their finite difference mesh. We also discretize only the overburden and, given the perfect conductor below, apply Neumann boundary conditions along the bottom of the mesh with Dirichlet conditions along the sides and top. To simulate the perfect conductor for the primary field computations, a conductivity of 10^{10} S m^{-1} was used. The TM mode results took 17 s to obtain on the PRIME 2655. An identical run took about 8 s on a VAX/780 (W. R. Sill,

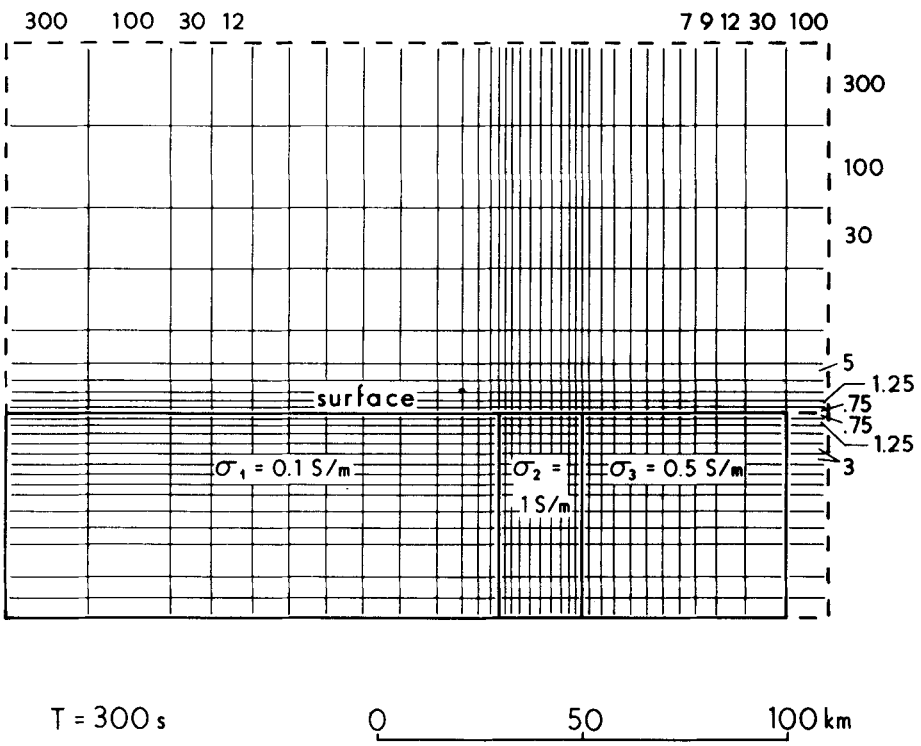

Figure 9. Finite element mesh discretization for the segmented overburden model. Heavy dashed lines indicate elements added to TM mode mesh in order to simulate TE mode response. Also, numerical labels near outer and upper groups of elements indicate modified element dimensions (in kilometres) to help validate Dirichlet boundary conditions and one-sided differencing for the TE mode calculations of Tables 3 and 4.

Table 1. Comparison of normalized magnetic induction and electric field at the surface ($z = 0$) from analytic (AN) and finite element (FE) calculations for TM polarization of segmented overburden model. Units of electric field are $V\,m^{-1}\,T^{-1}$.

$z = 0$

	B_x/B_{xo}				E_y/B_{xo}				E_z/B_{xo}			
y (km)	AN		FE		AN		FE		AN		FE	
	Re	Im	Re	Im	Re	Im	Re	Im	Re	Im	Re	Im
-52	1	0	1	0	-308	-292	-308	-292	0	0	0	0
-25	1	0	1	0	-322	-287	-321	-287	0	0	0	0
-15	1	0	1	0	-348	-303	-348	-303	0	0	0	0
-10(-)	1	0	1	0	-379	-366	-379	-363	0	0	0	0
-10(+)	1	0	1	0	-37.9	-36.6	-37.9	-36.3	0	0	0	0
-7	1	0	1	0	-59.4	-85.1	-60.0	-82.9	0	0	0	0
0	1	0	1	0	-83.4	-99.1	-84.6	-97.7	0	0	0	0
7	1	0	1	0	-82.1	-92.8	-83.1	-91.1	0	0	0	0
10(-)	1	0	1	0	-74.6	-75.3	-75.2	-74.2	0	0	0	0
10(+)	1	0	1	0	-149	-151	-150	-148	0	0	0	0
15	1	0	1	0	-138	-130	-139	-129	0	0	0	0
30	1	0	1	0	-129	-128	-130	-127	0	0	0	0
50	1	0	1	0	-129	-129	-130	-128	0	0	0	0

Table 2. Comparison of normalized fields at depth $z = 15$ km from analytic and finite element calculations for TM polarization of segmented overburden model.

$z = 15$ km

	B_x/B_{xo}				E_y/B_{xo}				E_z/B_{xo}			
y (km)	AN		FE		AN		FE		AN		FE	
	Re	Im	Re	Im	Re	Im	Re	Im	Re	Im	Re	Im
-52	.461	-.311	.461	-.311	-247	-66.6	-247	-66.6	.363	-2.88	.494	-2.93
-25	.443	-.298	.443	-.297	-250	-56.8	-250	-57.1	15.8	-2.66	16.6	-1.96
-15	.412	-.300	.412	-.299	-253	-44.9	-253	-45.4	37.0	7.69	37.5	8.14
-10(-)	.383	-.307	.383	-.307	-252	-30.5	-253	-31.0	55.2	17.7	55.0	17.7
-10(+)	.383	-.307	.383	-.307	-25.2	-3.05	-25.3	-3.10	55.2	17.7	55.4	17.0
-7	.205	-.341	.205	-.342	-23.2	6.30	-23.4	6.25	39.2	2.06	39.4	2.66
0	8.50×10^{-4}	-.302	-2.61×10^{-4}	-.303	-19.6	16.0	-19.9	15.9	9.81	-6.46	10.1	-6.22
7	-3.82×10^{-3}	-.263	-4.51×10^{-3}	-.264	-20.0	16.7	-20.3	16.5	-7.54	-2.21	-7.63	-2.32
10(-)	3.64×10^{-2}	-.257	3.62×10^{-2}	-.258	-21.8	14.6	-22.1	14.4	-13.8	-1.54	-13.9	-1.45
10(+)	3.64×10^{-2}	-.257	3.62×10^{-2}	-.258	-43.7	29.1	-44.3	28.7	-13.8	-1.54	-13.8	-1.51
15	7.07×10^{-2}	-.256	7.08×10^{-2}	-.257	-46.5	25.6	-47.0	25.1	-8.32	.847	-8.50	.699
30	.104	-.271	.105	-.272	-48.5	22.9	-48.9	22.5	-.746	1.34	-.817	1.34
50	.104	-.279	.105	-.279	-48.9	22.6	-49.2	22.1	.152	9.02×10^{-2}	.184	7.68×10^{-2}

Table 3. Comparison of normalized magnetic induction and electric field at the surface ($z = 0$) from analytic (AN) and finite element (FE) calculations for TE polarization of segmented overburden model. Units of electric field are $V m^{-1} T^{-1}$. The upper row of finite element results is for exactly the discretization of Weaver *et al.* (1986) while the lower is for the mesh modified according to the text and Fig. 9.

$z = 0$

	E_x/B_{xo}				B_y/B_{xo}				B_z/B_{xo}			
y (km)	AN		FE		AN		FE		AN		FE	
	Re	Im	Re	Im	Re	Im	Re	Im	Re	Im	Re	Im
-52	249	294	253 249	293 294	90.4	4.75	90.8 90.4	3.72 4.58	-28.8	69.7	28.3 29.8	71.7 70.4
-25	194	247	197 195	247 248	86.3	-1.60	86.6 86.3	-2.94 -1.74	-175	117	-180 -181	117 115
-15	171	196	174 172	196 196	92.9	-7.29	93.2 92.8	-8.17 -7.46	-335	87.5	-339 -339	88.0 84.9
-10	166	154	168 166	154 154	114	-3.09	114 114	-5.17 -3.72	-484	-8.0	-482 -491	-3.2 -16.0
- 7	162	129	164 162	128 129	129	-0.78	129 129	-3.67 -1.47	-321	90.6	-324 -324	91.1 88.3
0	147	102	148 147	101 102	131	-9.21	131 131	-11.9 -9.89	-79.3	92.1	-80.0 -80.9	92.6 91.6
7	138	102	139 138	101 102	124	-9.47	124 124	-12.1 -10.2	73.4	40.8	76.1 74.8	40.6 41.7
10	135	108	136 135	108 108	116	-9.89	116 116	-12.0 -10.5	146	54.0	146 149	53.7 58.0
15	133	120	134 133	120 120	106	-9.28	106 106	-10.8 -9.64	77.9	-0.1	80.9 79.8	0.4 1.1
30	136	130	138 136	130 130	103	-3.96	104 103	-5.29 -4.31	7.5	-8.0	9.3 8.0	-8.5 -8.3
50	137	130	138 137	131 130	103	-2.71	103 103	-3.60 -3.12	-1.8	2.1	1.4 -1.8	5.5 1.7

Table 4. Comparison of normalized fields at depth $z = 15$ km from analytic and finite element calculations for TE polarization of segmented overburden model.

z = 15 km

	E_x/B_{xo}				B_y/B_{xo}				B_z/B_{xo}			
y (km)	AN		FE		AN		FE		AN		FE	
	Re	Im	Re	Im	Re	Im	Re	Im	Re	Im	Re	Im
-52	206	86.7	207 206	84.7 86.5	43.3	-25.4	43.4 43.3	-26.1 -25.5	-4.8	67.5	-4.2 -5.7	69.1 68.6
-25	143	59.3	144 143	58.5 59.5	35.4	-23.9	35.5 35.6	-24.3 -23.9	-128	166	-132 -134	169 168
-15	102	19.5	103 102	18.8 19.6	24.4	-25.8	24.5 24.6	-26.2 -25.9	-264	230	-266 -267	235 232
-10	75.2	-13.0	75.6 75.4	-13.7 -13.1	12.6	-28.3	12.7 12.8	-28.7 -28.6	-359	285	-361 -362	290 286
-7	57.9	-30.1	57.9 58.0	-30.7 -30.2	4.98	-29.2	4.98 5.14	-29.6 -29.4	-193	259	-195 -197	261 259
0	30.1	-41.5	29.9 30.1	-42.0 -41.7	-3.32	-27.8	-3.34 -3.18	-28.1 -28.1	-0.8	111	-2.4 -3.3	112 112
7	24.8	-36.9	24.7 24.8	-37.2 -37.0	-2.54	-27.0	-2.52 -2.38	-27.4 -27.3	55.9	-34.4	57.0 57.1	-35.2 -34.5
10	28.6	-32.7	28.6 28.7	-33.0 -32.7	0.37	-27.2	0.42 0.56	-27.5 -27.4	79.0	-85.3	80.1 80.5	-86.9 -85.9
15	36.4	-26.5	36.5 36.5	-26.7 -26.4	5.10	-27.5	5.19 5.32	-27.8 -27.7	41.1	-63.0	42.3 42.7	-64.5 -63.6
30	48.0	-22.8	48.4 48.2	-23.0 -22.7	9.41	-28.6	9.52 9.60	-28.9 -28.7	-3.3	-16.6	-2.9 -3.1	-17.8 -17.3
50	50.2	-24.4	50.7 50.4	-24.2 -24.4	9.95	-29.0	10.3 10.2	-29.2 -29.0	-1.7	0.5	0.7 -2.2	0.8 - 0.1

private communication). Our values of B_x, E_y and E_z at $z = 0$ and $z = 15$ km, normalized by the primary magnetic induction B_{x0} at the surface, are listed in Tables 1 and 2 with the analytic response. The agreement is excellent as is that of Weaver *et al.* (1985).

The TE mode results from the finite element code are compared in Tables 3 and 4 to the analytic TE results provided by Weaver *et al.* (1986). The mesh used was the same as that for the TM excitation with the addition of one element column 10 km wide on the right side of a total size of 36×16 nodes. Agreement again is close overall; the most noticeable discrepancy is at the surface in the small imaginary component of B_y and in B_z at the contacts at $y = \pm 10$ km. Our solution seems fairly insensitive to whether an arctangent variation instead of a cosine taper is used for electric field boundary conditions in the air. The finite element solution for B_y appears improved if the sizes of the outer and upper groups of elements are increased substantially and if the element rows immediately bounding the ground surface are thinned to 0.75 km (Fig. 9, Tables 3 and 4). While the mesh size was still 36×16 nodes, these changes should help validate Dirichlet boundary conditions (cf. Weaver & Brewitt-Taylor 1978) and ensure that the one-sided differences (appropriate for topographic modelling) are fine enough. However, B_z at $z = 15$ km is only a bit improved from this and B_z at the surface in fact seems degraded slightly. TE mode run times were 43 s on the PRIME 2655 and 18 s on the VAX/780.

On the PRIME for this model, the secondary formulation and the original total-fields codes agreed to within 1 per cent amplitude and 1° phase at 300 s and also at 30 000 s for both modes. Matrix ill-conditioning was not a problem here very probably because the element aspect ratios of this mesh are modest compared with those of Fig. 1 and because results are not being calculated at extremely low induction numbers. Nevertheless, when modelling very broad band MT field data where both small and large structures figure in the response, extreme element dimensions often arise. Serious round-off error such as we have demonstrated with some meshes is much less likely for the finite difference code of Brewitt-Taylor & Weaver (1976) since they utilize double precision arithmetic throughout.

Conclusions

We have presented a numerical formulation which solves for the secondary field variations parallel to the strike of a 2-D body, plus the subsequent auxiliary fields. Calculating the secondary fields directly has overcome a difficulty with numerical accuracy at low frequencies for total field solutions utilizing single-precision arithmetic. The error in total field approaches manifests predominantly in the auxiliary fields and becomes unbounded as frequency falls. Such error should be considered also for inverse algorithms constructed using finite elements (e.g. Oristaglio & Worthington 1980). In addition to stability to ultra-low frequencies, use of single-precision arithmetic by our program results in a considerable saving of computer storage and execution time; calculation of the source vector is a negligible fraction of the effort. The mesh structure we have implemented allows input of mesh parameters which is as straightforward as that for finite difference methods while retaining the flexibility of triangular elements. As detailed by Wannamaker *et al* (1986), the latter are well suited for sloping boundaries and topography.

Acknowledgments

We are indebted to G. W. Hohmann for his insight and J. T. Weaver for his diligence in producing accurate solutions. Also we thank William R. Sill of the Montana College of Mineral Science and Technology for running the segmented overburden model on their

VAX 11/780. Further technical assistance came from S. Bromley, P. Daubner and J. Pingree. This work was supported by NSF grant EAR-8400248.

References

Brewitt-Taylor, C. R. & Weaver, J. T., 1976. On the finite difference solution of two-dimensional induction problems, *Geophys. J. R. astr. Soc.*, **47**, 375–396.

Coggon, J. H., 1971. Electromagnetic and electrical modelling by the finite element method, *Geophysics*, **36**, 132–155.

Hohmann, G. W., 1983. Three-dimensional EM modelling, *Geophys. Surveys*, **6**, 27–54.

Huebner, K. H. & Thornton, E. A., 1982. *The Finite Element Method for Engineers*, John Wiley, New York.

Kisak, E. & Sylvester, P., 1975. A finite element program package for magnetotelluric modelling, *Comput. Phys. Commun.*, **10**, 421–433.

Oristaglio, M. L. & Worthington, M. H., 1980. Inversion of surface and borehole electromagnetic data for two-dimensional electrical conductivity models, *Geophys. Prospect*, **28**, 633–657.

Rijo, J., 1977. Modelling of electric and electromagnetic data, *PhD thesis*, University of Utah.

Stodt, J. A., 1978. Documentation of a finite element program for solution of geophysical problems governed by the inhomogeneous 2-D scalar Helmholtz equation, *NSF Program Listing and Documentation*, University of Utah.

Strang, G. & Fix, F. J., 1973. *An Analysis of the Finite Element Method*, Prentice-Hall, Englewood Cliffs, New Jersey.

Swift, C. M., Jr, 1967. A magnetotelluric investigation of an electrical conductivity anomaly in the south-western United States, *PhD thesis*, Massachusetts Institute of Technology.

Wannamaker, P. E., Hohmann, G. W. & Ward, S. H., 1984. Magnetotelluric responses of three-dimensional bodies in layered earths, *Geophysics*, **49**, 1517–1533.

Wannamaker, P. E., Stodt, J. A. & Rijo, L., 1985. PW2D – finite element program for solution of magnetotelluric responses of two-dimensional earth resistivity structure: Program documentation, *University of Utah Research Institute Report ESL-158*.

Wannamaker, P. E., Stodt, J. A. & Rijo, L., 1986. Two-dimensional topographic responses in magnetotellurics modelled using finite elements, *Geophysics*, **51**, in press.

Ward, S. H., Peeples, W. J. & Ryu, J., 1973. Analysis of geoelectromagnetic data, *Meth. Comp. Phys.*, **13**, 163–238.

Weaver, J. T. & Brewitt-Taylor, C. R., 1978. Improved boundary conditions for the numerical solution of E-polarization problems in geomagnetic induction, *Geophys. J. R. astr. Soc.*, **54**, 309–317.

Weaver, J. T., LeQuang, B. V. & Fischer, G., 1985. A comparison of analytic and numerical results for a two-dimensional control model in electromagnetic induction – I. B-polarization calculations, *Geophys. J. R. astr. Soc.*, **82**, 263–277.

Weaver, J. T., LeQuang, B. V. & Fischer, G., 1986. A comparison of analytic and numerical results for a two-dimensional control model in electromagnetic induction – II. E-polarization calculations, *Geophys. J. R. astr. Soc.*, **87**, 917–948.